Chemical Science

ROYAL SOCIETY OF CHEMISTRY

EDGE ARTICLE

View Article Online
View Journal | View Issue

Cite this: *Chem. Sci.*, 2025, **16**, 14485

All publication charges for this article have been paid for by the Royal Society of Chemistry

Breaking the heavy-atom paradigm: weak-donor-engineered triplet harvesting in BODIPY photosensitizers for immunogenic pyroptosis therapy†

Hyeong Seok Kim,‡[ab] Hyeonji Rha,‡[a] Mohammad Izadyar,‡[ce] Supphachok Chanmungkalakul,[c] Haiqiao Huang,[d] Yi Young Kang,[b] Jae-Won Ka,[b] Yunjie Xu,*[a] Mingle Li,*[d] Xiaogang Liu*[c] and Jong Seung Kim*[a]

Boron-dipyrromethene (BODIPY)-based dyes emerge as promising agents for phototherapy; however, traditional methods to enhance spin–orbit coupling (SOC) through halogenation introduce dark toxicity and limit therapeutic applications. Here, we present a thiophene-bridged BODIPY functionalized scaffold with carbazole-benzothiophene (Cbz-Bth) substituents at the 2,6-positions. This design employs a weak yet semi-rigid donor to destabilize charge-transfer (CT) states, enabling T_2-mediated spin–orbit charge-transfer intersystem crossing (SOCT-ISC). The resulting photosensitizer, **Cbz-Bth-BDP**, demonstrates effective reactive oxygen species generation and the photocatalytic transformation of biomolecules such as nicotinamide adenine dinucleotide (NADH) and cytochrome c (Cyt c). Notably, **Cbz-Bth-BDP** induces pyroptosis by activating gasdermin E (GSDME), leading to cell swelling and the release of intracellular content. In a 3D tumor spheroid model, **Cbz-Bth-BDP** significantly inhibits tumor growth by reducing adenosine triphosphate (ATP) levels. This study highlights the advantages of accessing higher excited triplet states and positions **Cbz-Bth-BDP** as a promising, heavy-atom-free photosensitizer for cancer treatment through pyroptosis activation.

Received 13th May 2025
Accepted 14th July 2025

DOI: 10.1039/d5sc03466c

rsc.li/chemical-science

Introduction

Boron-dipyrromethene (BODIPY)-based organic dyes are widely recognized for their phototherapeutic potential due to their ease of modification, strong absorption properties, tunable quantum yields, and excellent biocompatibility.[1–5] In photodynamic therapy (PDT), a critical challenge is enhancing intersystem crossing (ISC) to efficiently populate the triplet state, thereby maximizing reactive oxygen species (ROS) production for cancer treatment.[1–5] Traditional strategies to improve ISC involve incorporating heavy atoms, such as bromine or iodine, at the 2,6-positions of the BODIPY core.[6–8] This enhances spin–orbit coupling (SOC) and facilitates singlet oxygen generation.[6–8] However, halogenated BODIPY photosensitizers (PSs) often lead to undesirable dark toxicity, limiting their therapeutic applications in biological systems.[9]

To mitigate these risks, non-halogenated BODIPY PSs have been explored as safer alternatives. Recent advances have focused on structural modifications to enhance ISC without heavy atoms.[10–12] Twisted BODIPY helicenes with distorted symmetry, for example, promote SOC-mediated ISC and show excellent PDT performance.[13–15] Similarly, rigid thiophene-fused BODIPYs, which incorporate sulfur atoms into the π-conjugated framework, enhance ISC by suppressing non-radiative decay pathways.[16–18] However, despite achieving higher quantum yields for triplet-state formation, their synthetic complexity, scalability, and limited tunability present significant barriers to their widespread use in diverse photodynamic applications.

Simpler strategies have emerged, including the development of heavy-atom-free BODIPY PSs by incorporating electron-rich aryl groups[19,20] or sterically hindered moieties at the meso-position of the BODIPY core.[21–23] Donor–acceptor–donor (D–A–D) systems with strong donors at the β-positions have also shown promise, improving ISC efficiency and ROS generation.[24] These systems rely on stable charge-transfer (CT) states that

[a]*Department of Chemistry, Korea University, Seoul, 02841, Korea. E-mail: jongskim@korea.ac.kr; xuyunjie87@korea.ac.kr*

[b]*Advanced Functional Polymers Research Center, Korea Research Institute of Chemical Technology Daejeon, 34114, Korea*

[c]*Fluorescence Research Group, Singapore University of Technology and Design, Singapore, 487372, Singapore. E-mail: xiaogang_liu@sutd.edu.sg*

[d]*College of Materials Science and Engineering, Shenzhen University, Shenzhen, 518060, China. E-mail: limingle@szu.edu.cn*

[e]*Research Center for Modeling and Computational Sciences, Faculty of Science, Ferdowsi University of Mashhad, Mashhad 9177948974, Iran*

† Electronic supplementary information (ESI) available. See DOI: https://doi.org/10.1039/d5sc03466c

‡ These authors contribute equally to this work.

reduce the energy gap between singlet (S_1) and triplet (T_1) states and increase SOC to promote ISC.[24,25] However, CT-state-based designs encounter inherent challenges. The rotational flexibility of substituents can result in undesirable reverse ISC and excessive non-radiative decay, compromising triplet-state quantum yields.[24,25] In highly polar aqueous environments, CT states may become overly stabilized, narrowing the energy gap between the S_1 (CT) and S_0 states.[26] This stabilization accelerates non-radiative decay (*via* the energy gap law), further reducing ISC efficiency. When the CT state energy drops below that of T_1, ISC can be inhibited, significantly diminishing therapeutic efficacy.

To address these challenges, we introduce a novel thiophene-bridged BODIPY scaffold featuring carbazole-benzothiophene (Cbz-Bth) substituents at the 2,6-positions. Unlike conventional approaches that rely on strong donors to enhance S_1–T_1 transitions, our strategy employs a weak yet semi-rigid donor. This design destabilizes the CT state, facilitating efficient ISC *via* a T_2-mediated pathway driven by a potent spin–orbit charge-transfer intersystem crossing (SOCT-ISC) mechanism. Comprehensive experimental and theoretical analyses reveal that the semi-rigid π-conjugated architecture not only narrows the S_1–T_2 energy gap but also optimizes ISC efficiency, leading to exceptional photocatalytic performance and robust ROS generation. Upon photoirradiation, irreversible oxidation of crucial biomolecules, *e.g.*, nicotinamide adenine dinucleotide (NADH), and the reduction of cytochrome c (Cyt c) from ferric (Fe^{3+}) to ferrous (Fe^{2+}) states (Scheme 1A and B), were also observed. Remarkably, **Cbz-Bth-BDP** triggers pyroptosis, a highly immunogenic form of programmed cell death (Scheme 1C).[27–29] These findings establish **Cbz-Bth-BDP** as a promising candidate for photo-controlled pyroptosis activation and offer a novel strategy for designing high-performance photosensitizers. By addressing non-radiative decay pathways and accessing higher excited triplet states, this work advances the potential of cancer phototherapy.

Results and discussion

Molecular design and synthesis of thiophene-bridged BODIPY PSs

We developed a series of thiophene-bridged BODIPY PSs by replacing traditional heavy atoms with thiophene-aminophenyl donors (Scheme S1†), aiming to enhance ISC to triplet states by leveraging the thiophene bridge.[30,31] The synthesis began with the coupling of borated triphenylamine with bromothiophene, followed by boration and Suzuki coupling with iodinated BODIPY to yield **TPA-th-BDP**. Further modifications involved conjugating carbazole and diphenylamine with benzothiophene, resulting in the final compounds, **Cbz-Bth-BDP** and **DP-Bth-BDP** (Scheme S2†). These compounds were thoroughly characterized by ^{1}H NMR, ^{13}C NMR, and LC-MS spectrometry, confirming their structures (Fig. S1–S17†).

Optical properties

The UV-vis and fluorescence spectra of the thiophene-bridged BODIPY PSs revealed maximum absorption wavelengths at 546, 532, and 529 nm for **TPA-th-BDP**, **DP-Bth-BDP**, and **Cbz-Bth-BDP**, respectively, making them suitable for green-light-activated phototherapy (Table 1 and Fig. 1B).

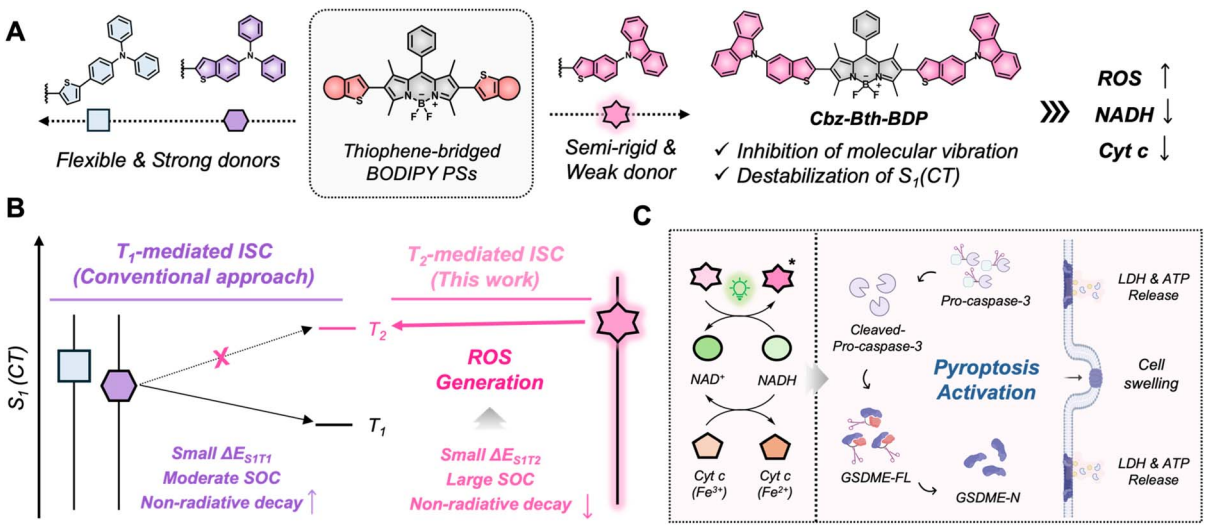

Scheme 1 Schematic illustration of newly developed BODIPY-based PSs. (A) Design and synthesis strategies for thiophene-bridged BODIPY PSs, focusing on enhancing photophysical and catalytic properties. The thiophene donors were meticulously engineered to restrict intramolecular motions, control electron-donating strength, and establish strong conjugation with the BODIPY core. (B) Weak donor-driven T_2-mediated SOCT-ISC mechanism: the carbazole-benzothiophene substituent destabilizes charge transfer in the singlet excited state, aligning it with the T_2 states to reduce the energy gap between S_1 and T_2. This enhances spin–orbit coupling SOC while minimizing non-radiative decay. Conversely, BODIPY derivatives with more flexible and stronger donors favor T_1-mediated ISC from S_1 to T_1, resulting in a larger energy gap, reduced SOC efficiency, and increased non-radiative decay. (C) **Cbz-Bth-BDP**-mediated pyroptosis activation: structural and photophysical enhancements enable robust ROS generation and efficient photoredox catalysis, positioning **Cbz-Bth-BDP** as a promising agent for pyroptosis-driven advanced phototherapeutic applications.

Table 1 Photophysical and photochemical properties of thiophene-bridged BODIPY PSs (**TPA-th-BDP**, **DP-Bth-BDP**, and **Cbz-Bth-BDP**)

BODIPY PSs	λ_{ex}[a] (nm)	ε[b] (M^{-1} cm^{-1})	λ_{em}[c] (nm)	ψ[d] (%)	HOMO[e] (eV)	LUMO[f] (eV)	E_g[g] (eV)	ΔE_{ST}[h] (eV)	SOC[i] (cm^{-1})	E_{ox}[j] (V)	E_{red}[k] (V)
TPA-th-BDP	546	49 950	623	27.3	−5.24	−3.19	2.05	0.25	1.29	0.832	−1.22
DP-th-BDP	532	28 940	595	16.5	−5.32	−3.14	2.18	2.18	3.45	0.917	−1.26
Cbz-Bth-BDP	529	52 320	614	51.7	−5.67	−3.45	−3.45	2.22	3.95	1.26	−0.96

[a] Maximum absorption wavelength of BODIPY PSs in THF. [b] Molar absorptivity at the maximum absorption wavelength. [c] Maximum absorption wavelength of BODIP PSs in THF. [d] Fluorescence quantum yield in THF. [e] Highest occupied molecular orbital (HOMO) level determined *via* cyclic voltammogram (CV). [f] Lowest unoccupied molecular orbital (LUMO) level determined *via* cyclic voltammogram (CV). [g] Energy band gap calculated from the HOMO and LUMO levels. [h] Singlet–triplet energy gap derived from density functional theory (DFT) calculations. [i] Spin orbital coupling (SOC) value obtained from DFT calculations. [j] Oxidation. [k] Reduction potentials determined by CV.

Correspondingly, their fluorescence emission maxima were observed at 623, 595, and 614 nm, respectively (Table 1 and Fig. S18–S20†). To investigate the substituents' optical properties, their ionization potential (IP) was then assessed, as lower IP values indicate stronger electron-donating effects. The electron-donating strength of the substituents followed the sequence: TPA-th (5.20 eV) > DP-Bth (5.24 eV) > Cbz-Bth (5.68 eV in water) (Fig. 1A and S22†). These findings align with the observed absorption peaks (λ_{abs}). Specifically, **Cbz-Bth-BDP**, with its weaker electron-donating carbazole-benzothiophene substituent, exhibited the shortest λ_{abs}, suggesting less effective intramolecular charge transfer (ICT). In contrast, **TPA-th-BDP**, with the strongest electron-donating substituent, exhibited the largest λ_{abs}, consistent with its lower IP value (Fig. 1B and S18–S20†).

Given the prominence of aminophenyl donors in aggregation-induced emission (AIE) chemistry,[25,32,33] we investigated whether these BODIPY PSs have AIE properties in aqueous solutions with varying fractions of THF (f_T). Interestingly, **Cbz-Bth-BDP** demonstrated significant fluorescence enhancement as the THF content increased from 0 to 99%. In contrast, under identical conditions, **TPA-th-BDP** only showed minimal fluorescence enhancement (Fig. S23†). **DP-Bth-BDP** exhibited the highest fluorescence intensity at a 10% THF fraction, although all BODIPY PSs displayed limited fluorescence in water (Fig. S23†). The fluorescence quantum yields of

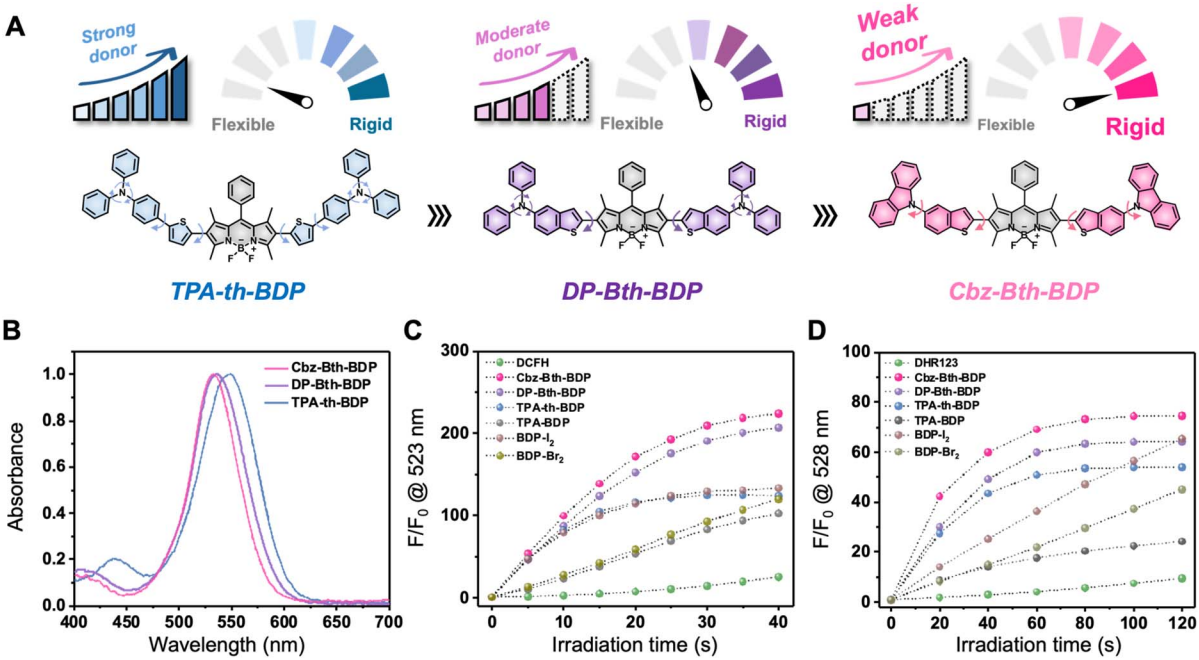

Fig. 1 Photophysical characteristics and ROS-generating capacity of BODIPY photosensitizers. (A) Molecular structures of thiophene-bridged BODIPY PSs. The thiophene donors are meticulously engineered to restrict intramolecular motions and are conjugated with the BODIPY core. Among these, the structure of **Cbz-Bth-BDP** effectively suppresses non-radiative decay, leading to low energy barriers between excited states (ΔE_{ST}) and promoting efficient ISC. (B) UV-vis absorbance spectra of thiophene-bridged BODIPY PSs (**TPA-th-BDP**, **DP-Bth-BDP**, and **Cbz-Bth-BDP**). (C and D) ROS production by BODIPY PSs (Conc. of PSs: 5 μM). Fluorescent changes of (C) DCFH (10 μM) and (D) DHR123 (10 μM) in PBS solution (10 mM, pH = 7.4, containing 10% DMSO) upon irradiation at 530 nm. The fluorescence ratio (F/F_0) for DCFH and DHR123 was measured at 523 nm (10 mW cm^{-2}, 5 s intervals) and 528 nm (100 mW cm^{-2}, 20 s intervals), respectively.

TPA-th-BDP, **DP-Bth-BDP**, and **Cbz-Bth-BDP** in THF solution were determined to be 27.3%, 16.5%, and 51.7%, respectively (Table 1). The superior quantum yield of **Cbz-Bth-BDP** can be attributed to its rigid molecular structure, which effectively suppresses non-radiative decay by restricting intramolecular motions (Fig. 1A).

ROS generation

ROS generation assays using DCFH (2,7-dichlorodihydrofluorescein) demonstrated that **Cbz-Bth-BDP** outperformed halogenated BODIPYs in ROS production, particularly under green-light irradiation. As depicted in Fig. 1C and S24,† **Cbz-Bth-BDP** showed the highest fluorescence increase at 523 nm under 530 nm irradiation (10 mW cm^{-2}), which was much higher than that of halogenated BODIPYs (BDP-Br_2 and BDP-I_2), indicating the robust ROS generation and the potential for heavy-atom-free biomedical applications. In contrast, **TPA-th-BDP** and **TPA-BDP** demonstrated minimal ROS generation, suggesting lower ISC efficiency. Interestingly, **Cbz-Bth-BDP** and **DP-Bth-BDP** also displayed excellent type I PDT activities to generate superoxide radicals, as illustrated in Fig. 1D and S25.† DHR123 (dihydrorhodamine 123) assay demonstrated **Cbz-Bth-BDP** and **DP-Bth-BDP** produced more superoxide radicals than halogenated BODIPY PSs under light irradiation (100 mW cm^{-2}), indicating **Cbz-Bth-BDP** may have the potential to work well under a hypoxic environment. Similarly, **Cbz-Bth-BDP** exhibited the highest fluorescence increase in the HPF assay (Fig. S26†), confirming efficient hydroxyl radical generation, consistent with previous reports on Fenton-like photocatalytic processes.[34–36] Next, we investigated the photoinduced singlet oxygen generation by BODIPY PSs in the ABDA assay (Fig. S27†). These findings were further supported by electron paramagnetic resonance (EPR) spectroscopy using spin-trapping agents: 5,5-dimethyl-1-pyrroline *N*-oxide (DMPO) for superoxide radicals, 5-*tert*-butoxycarbonyl-5-methyl-1-pyrroline-*N*-oxide (BMPO) for hydroxyl radicals, and 2,2,6,6-tetramethylpiperidine (TMPO) for singlet oxygen, verifying the efficient ROS production of **Cbz-Bth-BDP** samples (Fig. S28†).

To explore the influence of molecular aggregation on ROS generation under biologically relevant conditions, we examined the behavior of BODIPY PSs in monomeric (THF) and aggregated (distilled water) states. Aggregation is known to significantly impact the photophysical properties of photosensitizers.[37] Due to their limited solubility in water, thiophene-bridged BODIPYs likely exist in an aggregated form in aqueous environments. The DPBF (1,3-diphenylisobenzofuran) assay revealed markedly faster degradation in 100% distilled water under light irradiation, indicating enhanced ROS generation in the aggregated state of **Cbz-Bth-BDP** (Fig. S29A†). Similarly, the DHR123 assay demonstrated a notable fluorescence increase in water, reinforcing this observation (Fig. S29B†). These findings suggest that aggregation facilitates ISC, thereby optimizing ROS production for photodynamic applications. We further tested the photostability of our thiophene-bridged BODIPY PSs in aqueous environments. The compounds were subjected to continuous irradiation at 530 nm (100 mW cm^{-2}), and their UV-vis absorption spectra were recorded at 1-minute intervals (Fig. S30†). Compared to Rose Bengal (RB), a standard green-light photosensitizer that underwent significant photodegradation, the BODIPY derivatives exhibited remarkable spectral stability, maintaining their structural and optical integrity throughout the irradiation period. These results highlight the superior photostability of the BODIPY framework, emphasizing its potential for long-term photocatalytic applications.

DFT calculations and ISC mechanism

Enhancing the rigidity of the 2- and 6-substituents in BODIPY PSs is crucial for improving the ISC rates by reducing non-radiative decay caused by structural rotations.[24,25,38] Among the studied compounds, the structural flexibility follows the order of **TPA-th-BDP** > **DP-Bth-BDP** > **Cbz-Bth-BDP** (Fig. 1A). The highly rigid structure of **Cbz-Bth-BDP** minimizes non-radiative decay, thereby facilitating efficient ISC. To investigate the mechanisms underlying ROS generation in thiophene-bridged BODIPY PSs, we performed density functional theory (DFT) calculations to examine their singlet and triplet states. Geometry optimization and frontier molecular orbital (FMO) analysis revealed significant pre-twisting (>40°) of the thiophene (th) and benzothiophene (Bth) substituents relative to the BODIPY core, disrupting π-conjugation (Fig. S31†). For **Cbz-Bth-BDP**, the S_1 excitation corresponds to a locally excited (LE) state within the BODIPY fragment (*i.e.*, from HOMO to LUMO), while additional molecular orbitals introduced by the substituents suggest the potential for photoinduced electron transfer (PET) in the excited state (Fig. S32†).[38]

Comprehensive calculations of key photoexcitation and ISC states, including the Franck–Condon (FC), locally excited (LE), electron transfer (ET) singlet states, and triplet T_1(LE) and T_2(CT) states, demonstrated that photoexcitation primarily occurs within the BODIPY framework (Fig. 2A–C). In all three compounds, the S_1(ET) state was more stable than the S_1(LE) state, enabling a transition into the ET state and facilitating ISC *via* the SOCT-ISC mechanism. This mechanism is supported by stronger SOC between the S_1(ET) and T_1(LE)/T_2 (CT) states compared to the S_1(LE) and T_1(LE) states.[39,40]

Among the PSs, **Cbz-Bth-BDP** exhibited the most efficient ISC channels (Fig. 2A). Computational analysis revealed small singlet–triplet energy gaps (ΔE_{ST} < 0.30 eV) and large SOC values (>1.00 cm^{-1}) across all compounds (Fig. 2A–C). Notably, the S_1(ET) state of **Cbz-Bth-BDP** was exceptionally close to T_2(CT) state, with a ΔE_{ST} of only 0.02 eV (Fig. 2A), resulting in the highest SOC value of 3.95 cm^{-1}. In contrast, **DP-Bth-BDP** and **TPA-th-BDP** showed ΔE_{ST} values of 0.22 eV and 0.26 eV (Fig. 2D), respectively, with lower SOC values (3.45 cm^{-1} and 1.29 cm^{-1}) (Fig. 2E). These differences highlight the superior ISC efficiency of **Cbz-Bth-BDP**.

Experimental data in good solvents (*e.g.*, aqueous solutions containing 10% DMSO; Fig. 1C and D), align closely with these computational findings, underscoring the exceptional photosensitizing performance of **Cbz-Bth-BDP**. While aggregation is expected to enhance intermolecular interactions and further

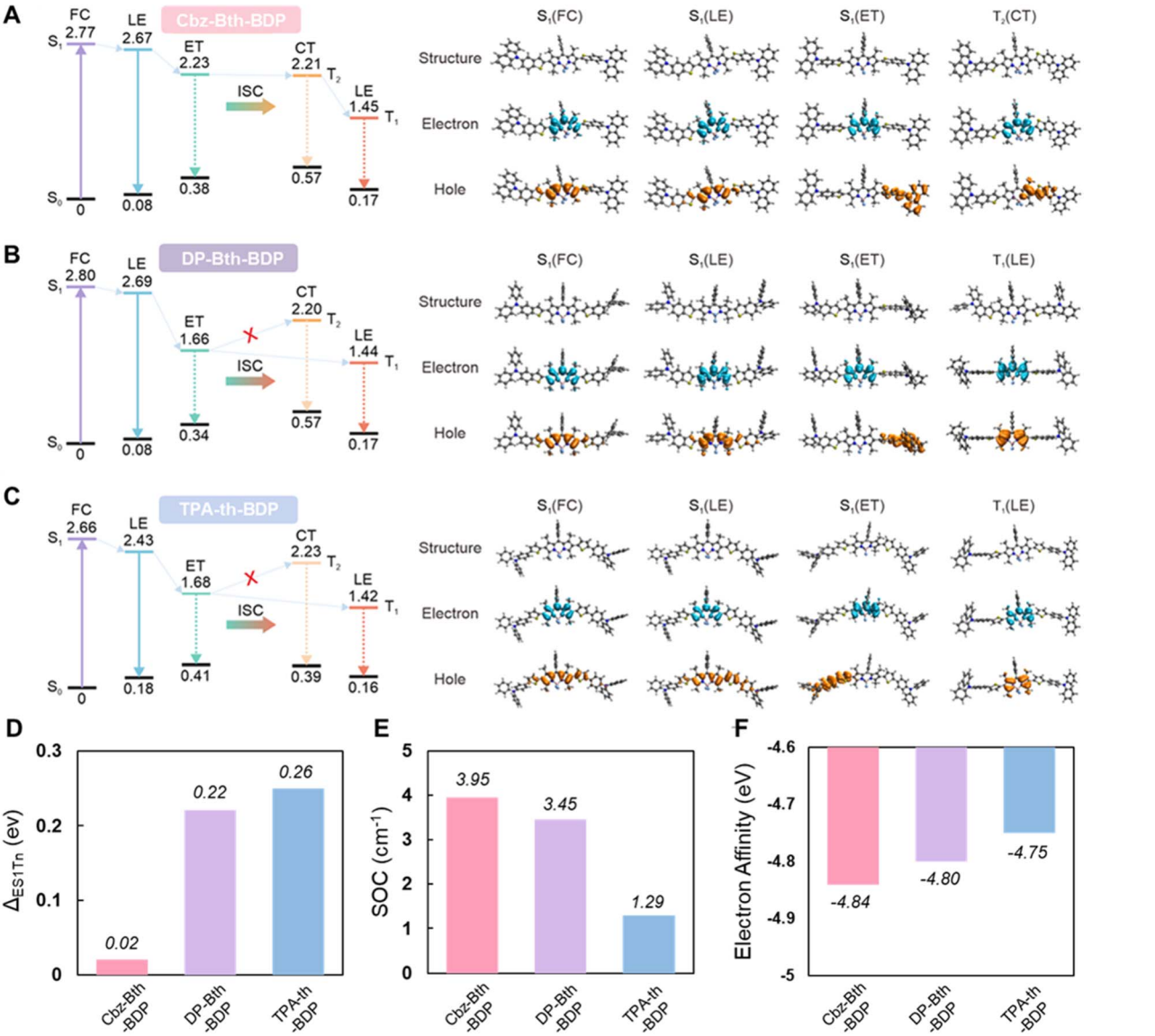

Fig. 2 Energy levels of key states, including the singlet Franck Condon (FC) state, locally excited (LE) state, electron transfer (ET) state, triplet LE, and charge-transfer (CT) states (T_1 and T_2). The molecular structures, and electron–hole distributions of S_1(FC), S_1(LE), S_1(ET), T_2(CT) and/or T_1(LE) states for (A) **Cbz-Bth-BDP**, (B) **DP-Bth-BDP**, and (C) **TPA-th-BDP**. (D) The singlet–triplet energy gap (ΔE_{ST}), (E) spin–orbit cupling (SOC) values, and (F) theoretical electron affinities of thiophene-bridged BODIPY PSs.

improve ISC and ROS generation, modeling such complex aggregates exceeds the computational capacity of detailed time-dependent DFT studies. Interestingly, upon reaching the T_1 state, all photosensitizers demonstrated significant electron affinity (<−4.70 eV), with **Cbz-Bth-BDP** showing the most negative value (Fig. 2F). These results suggest that **Cbz-Bth-BDP**, in particular, can effectively drive photocatalytic processes by accepting electrons from reductive biomolecules (*i.e.*, NADH).

Photoredox catalytic activities of Cbz-Bth-BDP

In photodynamic therapy, photoredox catalysis within live cells plays a new role in inducing cell death by mediating biomolecular conversion.[41] Reductive biomolecules like NADH can participate in the reductive cycling of photoexcited PSs, converting to its oxidative form (NAD^+) by single electron transfer (SET) (Fig. S33†).[42,43] To evaluate the photocatalytic activity of thiophene-bridged BODIPY PSs, we examined NADH oxidation under green light irradiation (530 nm, 100 mW cm^{-2}). The absorbance of NADH at 339 nm decreased over time, with new peaks appearing at 260 nm, confirming its oxidation (Fig. 3A). Among the BODIPYs, **Cbz-Bth-BDP** showed the most efficient photocatalytic conversion of NADH (Fig. 3B and S34†), consistent with its superior ROS generation and electron affinity. This enhanced photocatalytic efficiency is likely facilitated by aggregation-assisted photophysical effects, including improved triplet-state harvesting.[44,45]

Next, the cyclic voltammetry (CV) of thiophene-bridged BODIPYs was measured to demonstrate the feasibility of

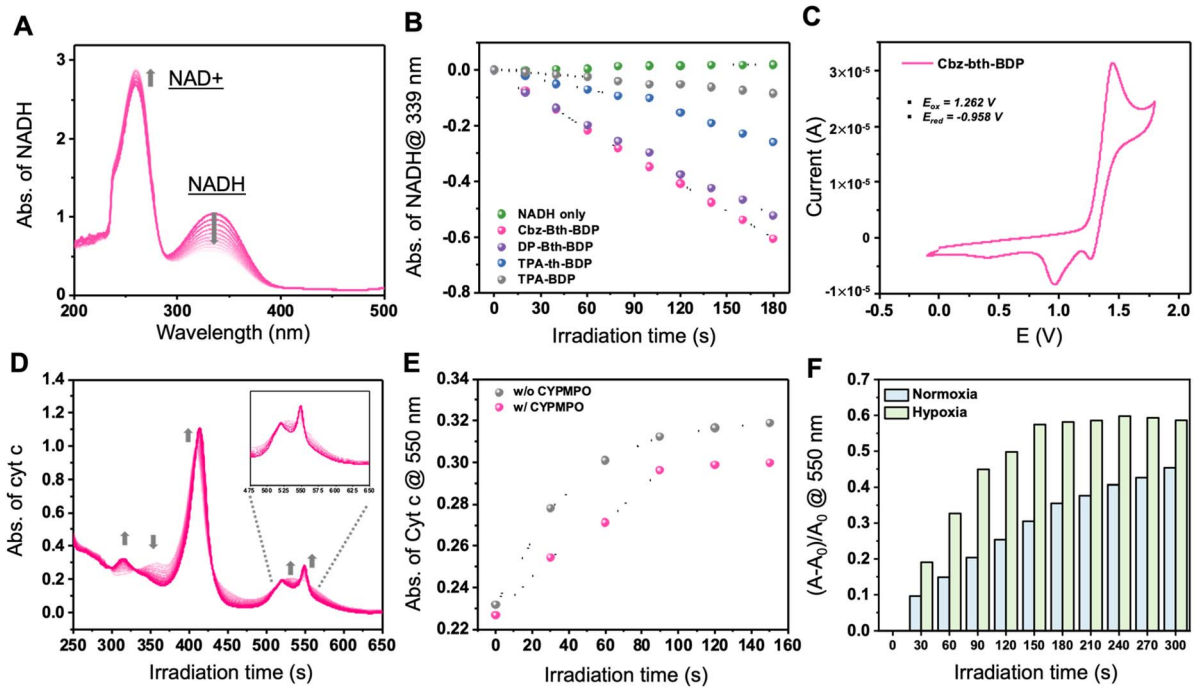

Fig. 3 Photocatalytic transformation of biological substrates. (A) Absorbance spectra for photocatalytic NADH (180 μM) oxidation. (B) Time-dependent plots of absorptive changes (A/A_0) at 339 nm, demonstrating the efficiency of NADH photooxidation by thiophene-bridged BODIPY PSs (**TPA-th-BDP**, **DP-Bth-BDP**, and **Cbz-Bth-BDP**) upon green light irradiation (100 mW cm^{-2}). (C) Cyclic voltammetry (CV) curves of **Cbz-Bth-BDP**. Inset: the values of oxidative and reductive potentials. (D) Absorption spectra showing the photocatalytic reductive transformation of Cyt c (Fe^{3+}) to Cyt c (Fe^{2+}) (10 μM) in the presence of **Cbz-Bth-BDP** (0.5 μM) and NADH (40 μM). The appearance of peaks at the β band (520 nm) and the α band (550 nm), two typical spectroscopic signatures of Cyt c (Fe^{2+}), indicates Cyt c (Fe^{3+}) reduction. (E) NAD$^{\bullet}$ trapping assay using CYPMPO under N_2 conditions. (F) Comparison of **Cbz-Bth-BDP**-mediated Cyt c photoreduction efficiency in aerobic (air) and deaerated (N_2) PBS solution.

electron transfer for photocatalytic NADH oxidation. As shown in Fig. 3C and S35,† the redox potentials of BODIPY PSs were determined as follows: **Cbz-Bth-BDP** ($E_{red} = -0.958$ V), **DP-Bth-BDP** ($E_{red} = -1.263$ V), and **TPA-th-BDP** ($E_{red} = -1.218$ V). The observed electrochemical trend in reduction potential closely aligns with our earlier theoretical calculations of electron affinity (Fig. 2F). Notably, the carbazole-benzothiophene substituents on **Cbz-Bth-BDP** notably enhanced its reduction potential, facilitating electron transfer from biological substrates. This enables oxygen-mediated reductive cycling, enabling **Cbz-Bth-BDP** as a promising candidate for NADH oxidation in photodynamic therapy.

Given that NADH can serve as an electron mediator, facilitating the reduction of mitochondrial electron carriers (*e.g.*, Cyt c) through oxygen-independent pathways, photoreduction offers a promising strategy for enhancing phototherapy.[46] In our study, we observed that the photocatalytic activity of BODIPY PSs played a crucial role in modulating the absorptive changes of Cyt c. Upon photo-irradiation, the characteristic β (520 nm) and α bands (550 nm) of Cyt c (Fe^{2+}) emerged in all BODIPY PSs, with **Cbz-Bth-BDP** showing the most pronounced spectral changes (Fig. 3D, S36 and S37†).

To confirm the generation of NAD radicals (NAD$^{\bullet}$) during the NADH-mediated photoreduction of Cyt c, we conducted CYPMPO assays. NAD$^{\bullet}$ trapping by CYPMPO inhibited Cyt c reduction, validating the radical's role in the process (Fig. 3E and S38†). Furthermore, a comparison of photoreduction in aerobic and nitrogen-purged solutions revealed greater Cyt c changes under deaerated conditions (Fig. 3F). In deaerated PBS, **Cbz-Bth-BDP** exhibited higher turn-over numbers (TON = 2.93) and turn-over frequency (TOF = 0.586 min^{-1}) compared to aerobic conditions (TON = 2.27, TOF = 0.454 min^{-1}) (Fig. S39†). These results emphasize the oxygen-independent photocatalytic activity of **Cbz-Bth-BDP**, showcasing its ability to disrupt cellular metabolism and its potential for phototherapy applications.

Photoexcited Cbz-Bth-BDP acts as a pyroptosis activator

With this highly effective heavy-atom-free BODIPY-based **Cbz-Bth-BDP** in hand, we investigated its photocatalytic mechanism in tumor cells. Under light irradiation (530 nm, 100 mW cm^{-2}) for 5, 10, and 15 min, **Cbz-Bth-BDP** induced cell death in a light-dose-dependent manner (Fig. S40†). Among all tested BODIPYs, **Cbz-Bth-BDP** showed the highest photocytotoxicity in MDA-MB-231 cells (Fig. 4A). Given NADH's critical role as a cofactor and redox component in tumor cells, we evaluated its interaction with **Cbz-Bth-BDP**. Maintaining the NADH/NAD^+ balance is essential for mitochondrial function and cellular metabolism.[47,48] Upon light irradiation, photoexcited **Cbz-Bth-BDP** led to a significant depletion of intracellular NADH levels compared to other BODIPY-based PSs (Fig. 4B). This reduction was further validated using the 3-(4,5-dimethylthiazo-2-yl)-2,5-

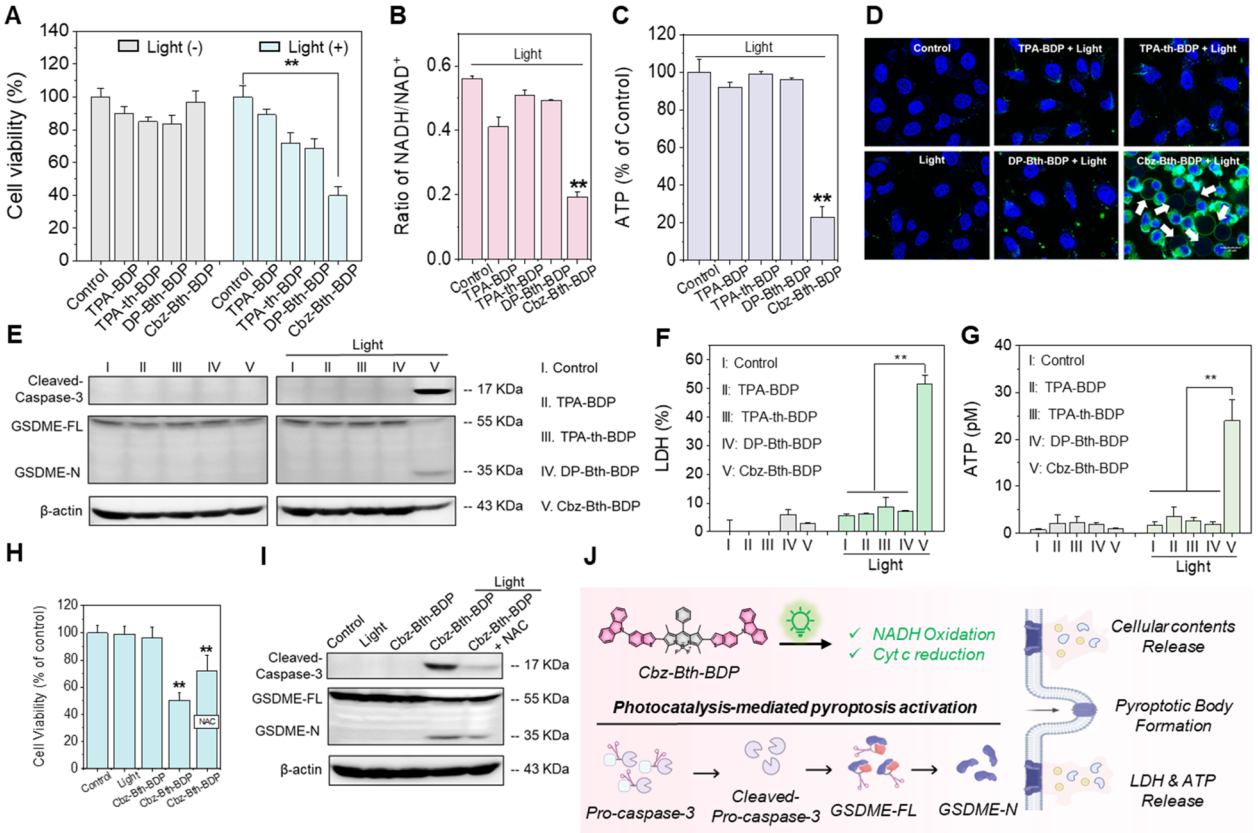

Fig. 4 Pyroptosis activation by photoexcited **Cbz-Bth-BDP**. (A) Cell viability of MDA-MB-231 cells treated with 2 μM BODIPY PSs under light irradiation (530 nm, 100 mW cm^{-2}, 10 min). (B) Alterations in the intracellular NADH/NAD^+ ratio and (C) ATP level in MDA-MB-231 cells following photoirradiation in the presence of BODIPY PSs. (D) Confocal laser microscopy images showing the pyroptotic morphology changes in MDA-MB-231 cells. The cell membrane is stained with FITC-Annexin-V (green), and the nucleus is stained with Hoechst 33342 (blue). White arrows indicate the pyroptotic bodies. Scale bar: 20 μm. (E) Western blot analysis of pyroptosis-related protein expression levels in MDA-MB-231 cells treated with BODIPY PSs and light irradiation. (F) Measurement of LDH and (G) ATP release into the supernatant of MDA-MB-231 cells treated with BODIPY PSs, both with and without light exposure. (H) Cell viability assays in the presence of ROS scavenger *N*-acetyl-L-cysteine (NAC), demonstrating the quenching of ROS generated by 2 μM **Cbz-Bth-BDP** under light irradiation. (I) Western blot assay showing pyroptosis-related protein expression after scavenging ROS with **Cbz-Bth-BDP** treatment. (J) Schematic representation of **Cbz-Bth-BDP**-mediated pyroptosis activation under light irradiation. Data are presented as mean ± SD ($n = 3$), $^*P < 0.05$, $^{**}P < 0.01$.

diphenyltetrazolium bromide (MTT) assay, which serves as an indirect indicator of intracellular NADH levels through MTT-formazan formation. Notably, post-irradiation, MTT-formazan formation was significantly reduced in **Cbz-Bth-BDP**-treated MDA-MB-231 cells relative to control groups, further validating the efficient photocatalytic conversion of NADH by **Cbz-Bth-BDP** (Fig. S41†). In the electron transport chain, NADH oxidation plays a crucial role in driving adenosine triphosphate (ATP) synthesis by generating a proton-motive force.[49] During oxidative phosphorylation, electrons from NADH are transferred through the electron transport chain, ultimately combining with O_2 to drive ATP synthesis. The oxidation of NADH to NAD^+ is a key energy-yielding reaction in this process. Consistent with this, ATP levels were markedly reduced in **Cbz-Bth-BDP**-treated cells under light irradiation compared to other PSs (Fig. 4C). This disruption of NADH/NAD^+ homeostasis by photoexcited **Cbz-Bth-BDP** underscores its photocatalytic impact, resulting in decreased ATP production.

Upon photoirradiation, **Cbz-Bth-BDP**-treated cells exhibited distinct pyroptotic morphological changes, setting them apart from conventional apoptosis. To confirm these morphological changes, we performed confocal laser scanning microscopy (CLSM) with dual staining using FITC-Annexin V (green), a phosphatidylserine (PS) marker for membrane disruption, and Hoechst 33342 (blue), a nuclear stain. Unlike apoptosis, which is typically characterized by cell shrinkage, nuclear condensation, and apoptotic body formation, **Cbz-Bth-BDP**-treated cells exhibited robust FITC-Annexin V binding while maintaining intact nuclei, reinforcing that the observed changes were pyroptotic rather than apoptotic (Fig. 4D). Notably, other BODIPY-based photosensitizers (PSs) failed to induce these morphological changes under identical conditions (Fig. S42†), highlighting the unique ability of **Cbz-Bth-BDP** to trigger pyroptosis. This distinct behavior is attributed to its enhanced photocatalytic activity and efficient ROS generation, which activate the pyroptotic cascade. These findings emphasize the unique mechanism of **Cbz-Bth-BDP** in driving pyroptotic cell death, further distinguishing it from conventional apoptosis-inducing photosensitizers.

Pyroptosis, a proinflammatory form of programmed cell death, is driven by the gasdermin protein family, which forms membrane pores upon activation.[27–29] Western blot assays confirmed that photoexcited **Cbz-Bth-BDP** triggered pyroptosis of MDA-MB-231 cells, evidenced by the upregulation of cleaved caspase-3 (active form of caspase 3) and GSDME-N (N-terminal fragment of gasdermin E, GSDME) (Fig. 4E and S43†). Moreover, the substantial release of lactate dehydrogenase (LDH) and ATP from **Cbz-Bth-BDP**-treated cells under photoirradiation (Fig. 4F and G) further provided additional evidence supporting the activation of pyroptosis. Additionally, confocal imaging of live/dead cell detection using calcein AM and propidium iodide (PI) assays supported these results. In this assay, live cells fluoresced green due to calcein AM, while dead cells emitted red fluorescence from PI staining. As shown in Fig. S44,† **Cbz-Bth-BDP**-treated cells displayed stronger red fluorescence after light exposure compared to other controls. Conversely, cells treated with other photosensitizers under similar conditions primarily exhibited green fluorescence. These findings position photoexcited **Cbz-Bth-BDP** as a highly effective and promising activator of pyroptosis among the heavy-atom-free thiophene-bridged BODIPYs.

To further evaluate the role of photocatalysis in **Cbz-Bth-BDP**-induced cell death, the ROS scavenger vitamin C (VC) was applied to neutralize ROS generated by **Cbz-Bth-BDP**. Pretreatment with VC reduced the cytotoxicity of **Cbz-Bth-BDP** under light irradiation compared to cells treated with **Cbz-Bth-BDP** alone. However, VC did not entirely prevent cell death, indicating that photocatalysis plays a significant role in **Cbz-Bth-BDP**-induced cytotoxicity (Fig. 4H). Western blot assays further confirmed that photoexcited **Cbz-Bth-BDP** could still trigger pyroptosis in the presence of VC, as evidenced by the upregulation of cleaved caspase-3 and GSDME-N (Fig. 4I and S45†). These findings underscore the critical role of the photocatalytic oxidation properties of **Cbz-Bth-BDP** in driving pyroptosis activation (Fig. 4J).

Photocatalytic activity of Cbz-Bth-BDP under hypoxic conditions

Photocatalytic therapy enables the direct oxidation of intracellular substrates *via* oxygen-independent pathways, thereby overcoming the inherent oxygen dependency in conventional phototherapy.[41,43] Given the remarkable photocatalytic

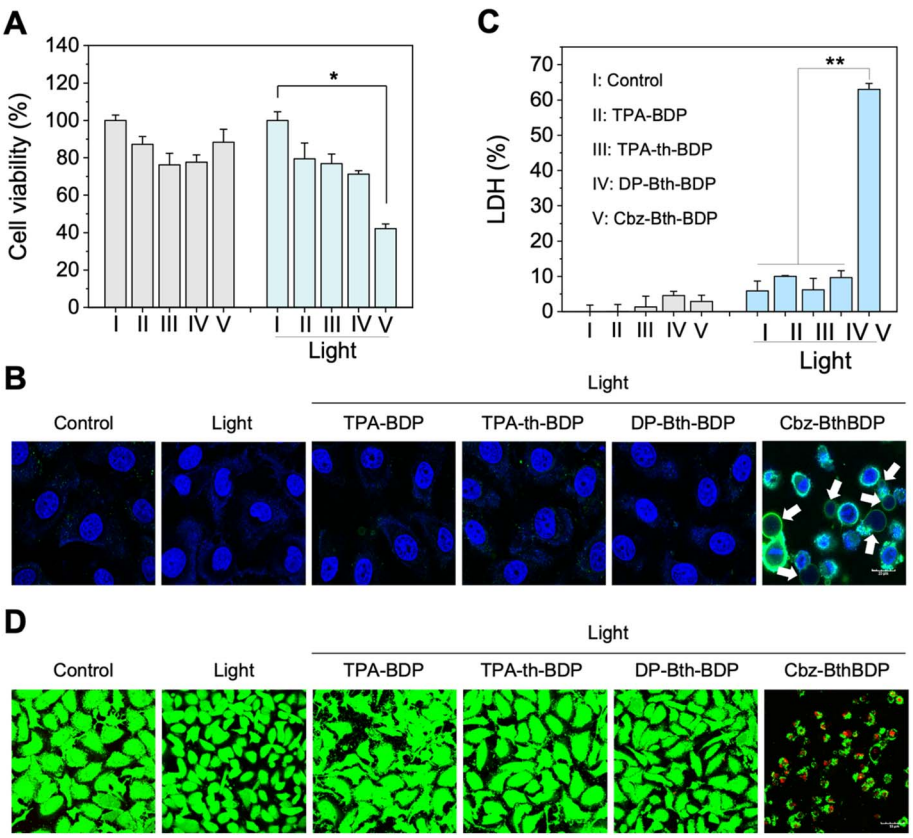

Fig. 5 (A) Cell viability of MDA-MB-231 cells under hypoxic conditions (2% O_2, 5% CO_2) with and without light exposure after treatment with (I) control, (II) **TPA-BDP**, (III) **TPA-th-BDP**, (IV) **DP-Bth-BDP**, and (V) **Cbz-Bth-BDP**. Cells were exposed to photoirradiation (green light, 100 mW cm^{-2}, 10 min), with each photocatalyst at a concentration of 2 μM. (B) Morphological features of pyroptotic MDA-MB-231 cells visualized by confocal laser microscopy under hypoxic conditions. Cells were stained with FITC-Annexin V (membrane marker) and Hoechst 33342 (nuclear marker). White arrows indicate pyroptotic bodies. Scale bars: 20 μm. (C) Measurement of lactate dehydrogenase (LDH) release into the supernatant of MDA-MB-231 cells following treatments. (D) Calcein AM and PI staining under hypoxic conditions. Calcein AM marks live cells (λ_{ex} = 473 nm and λ_{em} = 490–590 nm), while PI marks dead cells (λ_{ex} = 559 nm and λ_{em} = 575–675 nm). Data are presented as mean ± SD (n = 3), *P < 0.05, **P < 0.01.

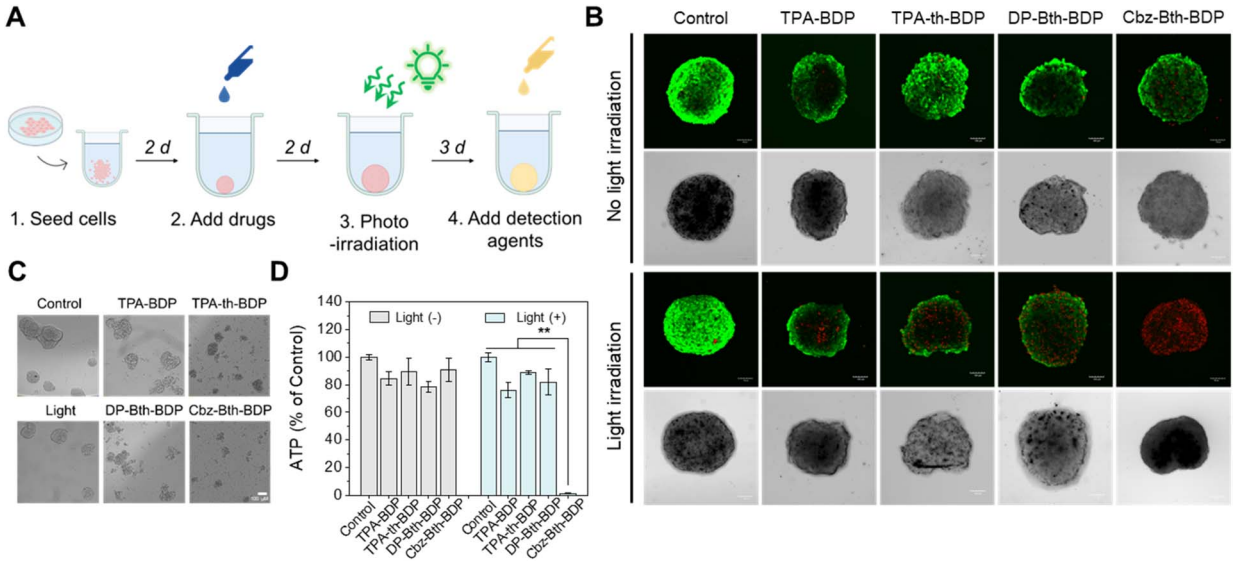

Fig. 6 Anticancer properties of **Cbz-Bth-BDP**. (A) Overview of the frame of the growth inhibition of **Cbz-Bth-BDP** on T47D 3D tumor spheroids. (B) Cell death of 3D tumor spheroids was detected by calcein AM/PI staining using confocal laser scanning microscopy (CLSM) imaging. (C) Tumor spheroid formation upon photoexcited **Cbz-Bth-BDP** treatment was evaluated using a tumor sphere formation assay. (D) Effect of **Cbz-Bth-BDP** on ATP level of tumor spheroid upon photoirradiation (530 nm PDT Lamp, 100 mW cm^{-2}, 20 min). Scale bars: 100 μm. Data are presented as mean ± SD ($n = 3$), $^{**}P < 0.01$.

performance of **Cbz-Bth-BDP** in normoxic conditions, we further evaluated its efficacy in hypoxic environments. The cytotoxicity of **Cbz-Bth-BDP** against MDA-MB-231 cells was assessed using the MTT assay. As shown in Fig. 5A, a concentration of 2 μM **Cbz-Bth-BDP** induced significant cytotoxicity under light irradiation (530 nm, 100 mW cm^{-2}, 10 min). In contrast, no cytotoxic effects were observed in cells treated with **Cbz-Bth-BDP** in the absence of light or with other PSs (**TPA-BDP**, **TPA-th-BDP**, and **DP-Bth-BDP**), irrespective of photoirradiation. Morphological changes in MDA-MB-231 cells after treatment with **Cbz-Bth-BDP** under light irradiation were further examined using the FITC-Annexin V/Hoechst 33342 staining assay. The cell membrane was stained with FITC-Annexin V, and the nucleus was stained with Hoechst 33342. After 10 min of light exposure (530 nm, 100 mW cm^{-2}), cells treated with **Cbz-Bth-BDP** displayed intense green fluorescence, indicating membrane damage and pyroptotic body formation. In contrast, cells treated with other PSs displayed only blue fluorescence, signifying intact cell membranes (Fig. 5B). To confirm these findings, LDH release was quantified using the CytoTox96™, non-radioactive cytotoxicity assay. Cells treated with **Cbz-Bth-BDP** showed substantial LDH release upon light irradiation, confirming significant membrane damage. In comparison, minimal LDH release was detected in cells treated with other PSs, regardless of light exposure (Fig. 5C). Additionally, a calcein AM/PI assay was conducted to further evaluate cell death. As shown in Fig. 5D, cells treated with **Cbz-Bth-BDP** and exposed to light (530 nm, 100 mW cm^{-2}, 10 min) exhibited strong red fluorescence, indicating effective cell death. Conversely, cells treated with other PSs under similar conditions predominantly exhibited green fluorescence. These results highlight the potent photocatalytic activity of **Cbz-Bth-BDP** in hypoxic conditions, demonstrating its potential as a promising candidate for antitumor therapy.

3D tumor spheroid model to probe anti-cancer effects

Three-dimensional (3D) multicellular spheroids are widely recognized as a reliable model for evaluating drug sensitivity due to their structural and functional resemblance to *in vivo* solid tumors.[50–52] Leveraging the potent photocatalytic properties of **Cbz-Bth-BDP**, we investigated its efficacy as an anticancer therapy using T47D breast cancer cell-derived 3D tumor spheroids (Fig. 6A). Upon treatment with **Cbz-Bth-BDP** and subsequent light irradiation, the spheroids exhibited significant cell death, as evidenced by confocal imaging with calcein AM (green, indicating live cells) and propidium iodide (PI, red, marking dead cells). In stark contrast, other BODIPY PSs displayed minimal cytotoxicity, regardless of photoirradiation (Fig. 6B). Additionally, photoactivated **Cbz-Bth-BDP** significantly inhibited the formation of T47D 3D spheroids compared to other PSs (Fig. 6C). This inhibition correlated with a substantial reduction in ATP production in the **Cbz-Bth-BDP**-treated group with light irradiation, highlighting its effective disruption of tumor spheroid metabolism (Fig. 6D). These findings highlight the potential of **Cbz-Bth-BDP** as a promising anticancer agent, demonstrating potent photocatalytic activity and significant therapeutic effects in a 3D tumor model.

Conclusion

In this study, we developed **Cbz-Bth-BDP**, a novel heavy-atom-free photosensitizer that leverages a weak yet semi-rigid donor to achieve highly efficient ISC through a T_2-mediated SOCT-ISC pathway. The incorporation of a weak donor strategically

destabilizes charge transfer in a singlet state, aligning it energetically with the T_2 states. This energy-level fine-tuning narrows the singlet–triplet energy gap, enhances spin–orbit coupling, and increases electron affinity, collectively boosting ISC efficiency and overall photocatalytic performance. The unique structural and photophysical properties of **Cbz-Bth-BDP** enable robust biological effects, including effective ROS generation, irreversible NADH oxidation, and cytochrome c transformation. These features drive pyroptosis *via* activating caspase 3 and GSDME, inducing cell death even under hypoxic conditions. Additionally, **Cbz-Bth-BDP** demonstrates significant anticancer potential by effectively inhibiting the growth of 3D tumor spheroids. While the current study establishes a strong foundation for **Cbz-Bth-BDP**'s pyroptosis-mediated cancer immunotherapy, its *in vivo* application remains limited by high-energy absorption and short excitation wavelengths. Future research will focus on molecular engineering strategies to extend absorption into the red/NIR region, improve tissue penetration, and enhance biocompatibility, ultimately facilitating clinical translation. Overall, this work presents **Cbz-Bth-BDP** as a promising next-generation photosensitizer, offering a transformative strategy for pyroptosis-mediated cancer therapy and expanding the frontier of photocatalytic cancer immunotherapy.

Data availability

Detailed synthetic schemes, experimental procedures, theoretical calculations, and other figures are provided in the ESI file.†

Author contributions

Y. X., M. L., X. L., and J. S. K. conceived and supervised the study. H. S. K. contributed to the experimental design and manuscript writing. H. S. K. and H. R. performed the synthetic work and characterized the optical properties. Y. X. and H. R. carried out the anticancer mechanisms. M. I. and S. C. carried out the computational studies. H. H. and Y. Y. K. assisted with material preparation and characterization. J.-W. K. assisted with manuscript editing and revision. All authors discussed the results and provided comments on the manuscript.

Conflicts of interest

There are no conflicts to declare.

Acknowledgements

We gratefully acknowledge the financial support from the National Research Foundation of Korea (CRI project no. 2018R1A3B1052702, J. S. K.; RS-2023-00241100, Y. X.). This work is also supported by the Ministry of Education, Singapore (MOE-T2EP10222-0001), Singapore University of Technology and Design (SUTD) Kickstarter Initiative (SKI 2021_03_10), National Natural Science Foundation of China (Grant No. 22308220, M. L.; No. 82203050, Y. X.), Province Key Areas Special Project for Regular Colleges and Universities (Grant No. 2024ZDZX2018, M. L.), Shenzhen University Third-Phase Project of Constructing High-Level University (Grant No. 000001032104, M. L.), Research Team Cultivation Program of Shenzhen University (Grant No. 2023QNT005, M. L.), and KRICT core project (KS2321-20). The authors are grateful for the computing service of SUTD and the National Supercomputing Centre (Singapore).

References

1 H. Cheng, X. Cao, S. Zhang, K. Zhang, Y. Cheng, J. Wang, J. Zhao, L. Zhou, X. Liang and J. Yoon, *Adv. Mater.*, 2023, **35**, 2207546.
2 B.-K. Liu, J. Zheng, H. Wang, L.-Y. Niu and Q.-Z. Yang, *Mater. Chem. Front.*, 2023, **7**, 5879–5890.
3 J. Wang, Q. Gong, L. Jiao and E. Hao, *Coord. Chem. Rev.*, 2023, **496**, 215367.
4 E. Bassan, A. Gualandi, P. G. Cozzi and P. Ceroni, *Chem. Sci.*, 2021, **12**, 6607–6628.
5 A. Kamkaew, S. H. Lim, H. B. Lee, L. V. Kiew, L. Y. Chung and K. Burgess, *Chem. Soc. Rev.*, 2013, **42**, 77–88.
6 Z. Fan, K. Teng, Y. Xu, L. Niu and Q. Yang, *Angew. Chem., Int. Ed.*, 2025, **64**, e202413595.
7 M. Won, S. Koo, H. Li, J. L. Sessler, J. Y. Lee, A. Sharma and J. S. Kim, *Angew. Chem., Int. Ed.*, 2021, **60**, 3196–3204.
8 H. S. Jung, J. Han, H. Shi, S. Koo, H. Singh, H.-J. Kim, J. L. Sessler, J. Y. Lee, J.-H. Kim and J. S. Kim, *J. Am. Chem. Soc.*, 2017, **139**, 7595–7602.
9 J. Zou, Z. Yin, K. Ding, Q. Tang, J. Li, W. Si, J. Shao, Q. Zhang, W. Huang and X. Dong, *ACS Appl. Mater. Interfaces*, 2017, **9**, 32475–32481.
10 S. Mula and M. Koli, *ChemMedChem*, 2024, **19**, e202400041.
11 M. A. Filatov, *Org. Biomol. Chem.*, 2020, **18**, 10–27.
12 X. Xiao, K. Ye, M. Imran and J. Zhao, *Appl. Sci.*, 2022, **12**, 9933.
13 X. Shi, Y. Wang, F. Qi, H. Zhang, Y. Cao, X. Xu, W. Liu and C. Li, *Small*, 2024, **20**, 2405496.
14 W. Li, Q. Gong, Q. Wu, L. Guo, X. Guo, D. Guo, L. Jiao and E. Hao, *Chem. Commun.*, 2023, **59**, 12330–12333.
15 Y. Dong, B. Dick and J. Zhao, *Org. Lett.*, 2020, **22**, 5535–5539.
16 X. Fu, Y. Man, C. Yu, Y. Sun, E. Hao, Q. Wu, A. Hu, G. Li, C.-C. Wang and J. Li, *J. Org. Chem.*, 2024, **89**, 4826–4839.
17 W. Bu, C. Yu, Y. Man, J. Li, Q. Wu, S. Gui, Y. Wei, L. Jiao and E. Hao, *Chem. Commun.*, 2024, **60**, 9809–9812.
18 S. Qi, N. Kwon, Y. Yim, V.-N. Nguyen and J. Yoon, *Chem. Sci.*, 2020, **11**, 6479–6484.
19 J. M. Lee, J. M. Park, H. K. Lee, H. M. Kim, J. H. Kim and J. P. Kim, *Dyes Pigm.*, 2021, **196**, 109662.
20 Y. Hou, Q. Liu and J. Zhao, *Chem. Commun.*, 2020, **56**, 1721–1724.
21 P. Zhao, Z. Wang, Y. Wang, Z. Wu, Y. Guo, C. Wang, X. Fang, Z. Qu, H. Wang and G. Zhao, *Dyes Pigm.*, 2023, **214**, 111214.
22 S. Callaghan, M. A. Filatov, H. Savoie, R. W. Boyle and M. O. Senge, *Photochem. Photobiol. Sci.*, 2019, **18**, 495–504.
23 M. A. Filatov, S. Karuthedath, P. M. Polestshuk, S. Callaghan, K. J. Flanagan, M. Telitchko, T. Wiesner, F. Laquai and M. O. Senge, *Phys. Chem. Chem. Phys.*, 2018, **20**, 8016–8031.

24 V. Nguyen, Y. Yim, S. Kim, B. Ryu, K. M. K. Swamy, G. Kim, N. Kwon, C. Kim, S. Park and J. Yoon, *Angew. Chem., Int. Ed.*, 2020, **59**, 8957–8962.
25 F.-Z. Xu, L. Zhu, H.-H. Han, J.-W. Zou, Y. Zang, J. Li, T. D. James, X.-P. He and C.-Y. Wang, *Chem. Sci.*, 2022, **13**, 9373–9380.
26 A. Uddin, S. R. Allen, A. K. Rylski, C. J. O'Dea, J. T. Ly, T. A. Grusenmeyer, S. T. Roberts and Z. A. Page, *Angew. Chem., Int. Ed.*, 2023, **62**, e202219140.
27 K. Wang, Q. Sun, X. Zhong, M. Zeng, H. Zeng, X. Shi, Z. Li, Y. Wang, Q. Zhao, F. Shao and J. Ding, *Cell*, 2020, **180**, 941–955.
28 M. Jiang, L. Qi, L. Li and Y. Li, *Cell Death Discov.*, 2020, **6**, 112.
29 S. Rühl, K. Shkarina, B. Demarco, R. Heilig, J. C. Santos and P. Broz, *Science*, 2018, **362**, 956–960.
30 X. Yang, X. Wang, X. Zhang, J. Zhang, J. W. Y. Lam, H. Sun, J. Yang, Y. Liang and B. Z. Tang, *Adv. Mater.*, 2024, **36**, 2402182.
31 P. Xiao, Z. Shen, D. Wang, Y. Pan, Y. Li, J. Gong, L. Wang, D. Wang and B. Z. Tang, *Adv. Sci.*, 2022, **9**, 2104079.
32 F. Ma, S. Zhang, J. Jiang, Y. Liu, J. Sun, J. W. Y. Lam, Z. Zhao and B. Z. Tang, *Adv. Mater.*, 2025, **37**, 2414188.
33 Z. Li, B. Z. Tang and D. Wang, *Adv. Mater.*, 2024, **36**, 2406047.
34 C. Lee, M. Park, W. C. B. Wijesinghe, S. Na, C. G. Lee, E. Hwang, G. Yoon, J. K. Lee, D.-H. Roh, Y. H. Kwon, J. Yang, S. A. Hughes, J. E. Vince, J. K. Seo, D. Min and T.-H. Kwon, *Nat. Commun.*, 2024, **15**, 4025.
35 H. Huang, S. Banerjee, K. Qiu, P. Zhang, O. Blacque, T. Malcomson, M. J. Paterson, G. J. Clarkson, M. Staniforth, V. G. Stavros, G. Gasser, H. Chao and P. J. Sadler, *Nat. Chem.*, 2019, **11**, 1041–1048.
36 Z. Zhao, *Free Radic. Biol. Med.*, 2023, **208**, 510–515.
37 Y.-F. Kang, W.-K. Chen, K.-X. Teng, L.-Y. Wang, X.-C. Xu, L.-Y. Niu, G. Cui and Q.-Z. Yang, *CCS Chem.*, 2022, **4**, 3516–3528.
38 W. Chi, J. Dai, C. Yan, D. Tan, Z. Guo and X. Liu, *J. Mater. Chem. C*, 2023, **11**, 10205–10214.
39 W. Chi, J. Chen, W. Liu, C. Wang, Q. Qi, Q. Qiao, T. M. Tan, K. Xiong, X. Liu, K. Kang, Y.-T. Chang, Z. Xu and X. Liu, *J. Am. Chem. Soc.*, 2020, **142**, 6777–6785.
40 J. T. Buck, A. M. Boudreau, A. DeCarmine, R. W. Wilson, J. Hampsey and T. Mani, *Chem*, 2019, **5**, 138–155.
41 M. Li, Y. Xu, Z. Pu, T. Xiong, H. Huang, S. Long, S. Son, L. Yu, N. Singh, Y. Tong, J. L. Sessler, X. Peng and J. S. Kim, *Proc. Natl. Acad. Sci. U. S. A*, 2022, **119**, e2210504119.
42 Y. Xu, C. V. Chau, J. Lee, A. C. Sedgwick, L. Yu, M. Li, X. Peng, J. S. Kim and J. L. Sessler, *Proc. Natl. Acad. Sci. U. S. A*, 2024, **121**, e2314620121.
43 M. Li, K. H. Gebremedhin, D. Ma, Z. Pu, T. Xiong, Y. Xu, J. S. Kim and X. Peng, *J. Am. Chem. Soc.*, 2022, **144**, 163–173.
44 N. Zhang, S. Trépout, H. Chen and M.-H. Li, *J. Am. Chem. Soc.*, 2023, **145**, 288–299.
45 K.-X. Teng, L.-Y. Niu, N. Xie and Q.-Z. Yang, *Nat. Commun.*, 2022, **13**, 6179.
46 L. Yu, Y. Xu, Z. Pu, H. Kang, M. Li, J. L. Sessler and J. S. Kim, *J. Am. Chem. Soc.*, 2022, **144**, 11326–11337.
47 R. P. Goodman, A. L. Markhard, H. Shah, R. Sharma, O. S. Skinner, C. B. Clish, A. Deik, A. Patgiri, Y.-H. H. Hsu, R. Masia, H. L. Noh, S. Suk, O. Goldberger, J. N. Hirschhorn, G. Yellen, J. K. Kim and V. K. Mootha, *Nature*, 2020, **583**, 122–126.
48 C. Cantó, K. J. Menzies and J. Auwerx, *Cell Metab.*, 2015, **22**, 31–53.
49 H. Li, S. K. Kolluri, J. Gu, M. I. Dawson, X. Cao, P. D. Hobbs, B. Lin, G. Chen, J. Lu, F. Lin, Z. Xie, J. A. Fontana, J. C. Reed and X. Zhang, *Science*, 2000, **289**, 1159–1164.
50 S. A. Saemundsson, S. D. Curry, B. M. Bower, E. J. DeBoo, A. P. Goodwin and J. N. Cha, *Biomater. Sci.*, 2024, **12**, 4759–4769.
51 E. C. Costa, A. F. Moreira, D. De Melo-Diogo, V. M. Gaspar, M. P. Carvalho and I. J. Correia, *Biotechnol. Adv.*, 2016, **34**, 1427–1441.
52 J. Friedrich, C. Seidel, R. Ebner and L. A. Kunz-Schughart, *Nat. Protoc.*, 2009, **4**, 309–324.